JUSTUS-LIEBIG-UNIVERSITÄT GIESSEN

Bachelor Thesis

Validation of the light yield nonlinearity implementation for EMC crystals in the PandaRoot simulation framework

Implementationsvalidierung der nichtlinearen Lichtausbeute der EMC-Kristalle im PandaRoot Framework

submitted by:
Simon Glennemeier-Marke

Reviewer:
Prof. Kai-Thomas Brinkmann
Prof. Claudia Höhne

Supervisor:
Dr. Markus Moritz
Dr. Hans-Georg Zaunick

Justus-Liebig-University, Giessen
II. Institute of Physics

February 6, 2023

Abstract

The PandaRoot simulation framework is a simulation environment used to model the operation of the future $\overline{\mathrm{P}}$ANDA detector, which is being build at the antiproton collider FAIR/GSI facility in Darmstadt. The $\overline{\mathrm{P}}$ANDA detector is composed of several subdetectors, each providing a subset of information used to reconstruct the collision event. One of these subdetectors, the Electromagnetic Calorimeter (EMC), uses tapered lead tungstate crystals as the sensitive detector volume. Due to their tapering, these crystals show nonlinear light collecting behavior when scintillation light is created at various positions along the length of the crystal. This effect is implemented in the simulation framework PandaRoot, which is used to test and develop analysis algorithms. The probing of the light yield in situ, i.e. using the full PandaRoot toolchain without a dedicated, pure Geant4 simulation, is the focus of this work. Unfortunately the results are inconclusive, as conflicting experimental data both confirms and disproves the validity of the current implementation. More experimental data is needed to resolve this conflict.

Table of Contents

1 Introduction

The Facility for Antiproton and Ion Research (FAIR) is a new particle accelerator facility currently under construction in Darmstadt, Germany. The main research topics will be covered by its four collaborations: Nuclear Structure, Astrophysics and Reactions (NUSTAR), Compressed Baryonic Matter (CBM), Atomic, Plasma Physics and Applications (APPA) and Antiproton Annhilation at Darmstadt ($\overline{\text{P}}$ANDA). The $\overline{\text{P}}$ANDA collaboration and its experiment will aim to gather more information about the strong force using the annihilation of antiprotons. Another field of interest is the generation of hadronic masses, which for the nuclei, is about 50 times larger than the masses of their constituents. The large energy that is released in the annhilation of the antiprotons will help to create conditions where new insights may be found.

In order to reconstruct the primary event from the fragments that were produced by the collision, one needs precise data on the momentum of the resulting fragments. This is the task of the Electromagnetic Calorimeter (EMC). The sensitive volumes of this detector consist of tapered lead tungstate crystals ($PbWO_4$, PWO-II).

The tapering of the crystals has a strong influence on the amount of light collected by the Avalanche Photodiodes (APDs) due to focussing effects. In order to accurately determine the incident particle energies, this nonlinearity of the light yield needs to be understood.

The PandaRoot simulation framework is used to simulate the operation of the whole $\overline{\text{P}}$ANDA detector. Using the simulated detector as a realistic source of raw experiment data, online reconstruction and particle identification algorithms can then be developed. This simulation package is called PandaRoot and it is built on ROOT and Virtual Monte Carlo (VMC) packages. To achieve realistic detector responses, effects such as the light yield nonlinearity of the crystals were implemented in previous development stages of the PandaRoot framework. This thesis will focus on testing and validating these implementation.

2 The $\overline{\text{P}}$ANDA EMC

2.1 Antiproton production at FAIR

Antiprotons are produced in the inelastic collisions of 29 GeV protons from the heavy ion synchrotron SIS100 with a metal target, such as Copper or Nickel [1] ('$\overline{\text{p}}$ target' in Figure 2.1). Particles generated in the collisions are collected and filtered for antiprotons in the subsequent Collector Ring (CR). After the CR, the High Energy Storage Ring (HESR) further accelerates or decelerates the antiprotons to the desired energies of up to 15 GeV.

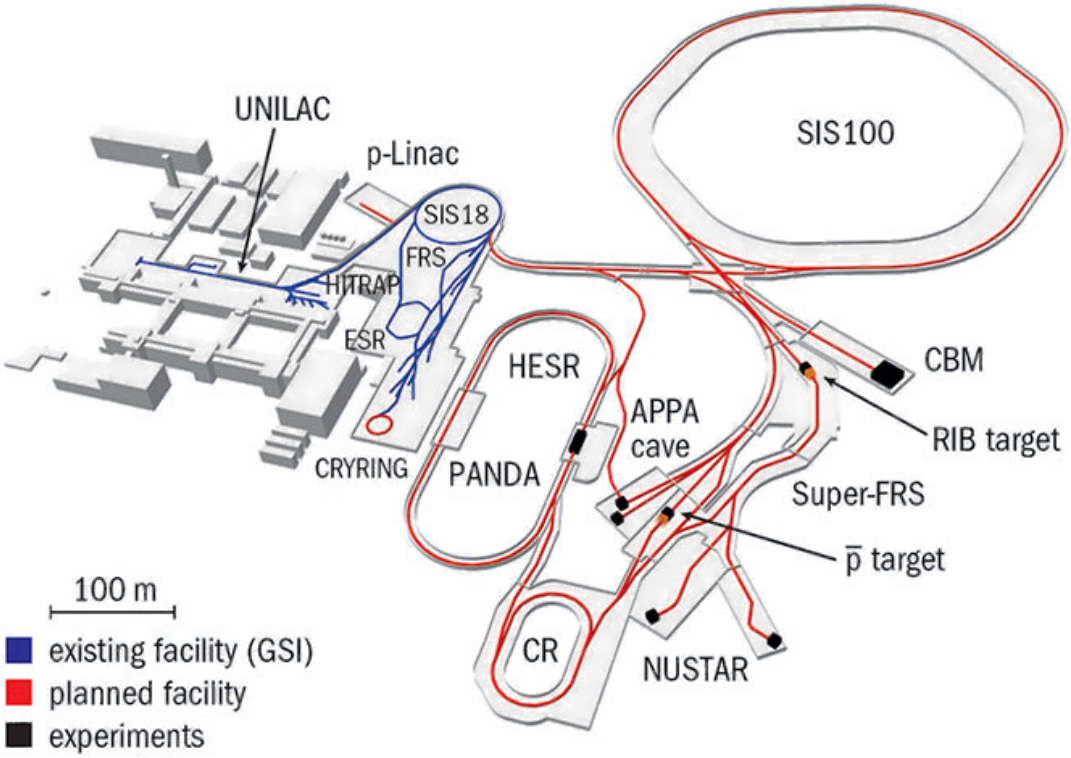

Figure 2.1: Schematic overview drawing of the FAIR site.

2.2 $\overline{\text{P}}$ANDA Experiment

The $\overline{\text{P}}$ANDA experiment is located at the HESR. It is a fixed target experiment and $\overline{\text{P}}$ANDA is therefore divided into the Target Spectrometer (TS) and Forward Spectrometer (FS). Targets for the collision are injected from the top of the detector and can either be solid pellets or dense clusters of target gas such as hydrogen or heavier gases such as deuterium, nitrogen or argon [2]. In order to provide a coverage as close to 4π as possible, the TS is constructed in a compact shell like structure, similar to other collider experiments such ATLAS or CMS. Starting from the target vertex going outward, the TS is composed of the following subdetectors: Micro-Vertex-Detector (MVD), Straw Tube Tracker (STT), Detection of Internally Reflected Cherenkov light (DIRC) and EMC. Additionally, a muon range system is incorporated into the magnetic yoke. It consits of a stack of muon detecting plates and iron plates. The main purpose of the iron plates is to guide the magnetic field, generated by superconducting magnets. Additionally they act as absorber plates for charged particles. The intermediate plates of the muon range system then determine how many plates a particle has penetrated, thus providing an energy estimate of the incident particle.

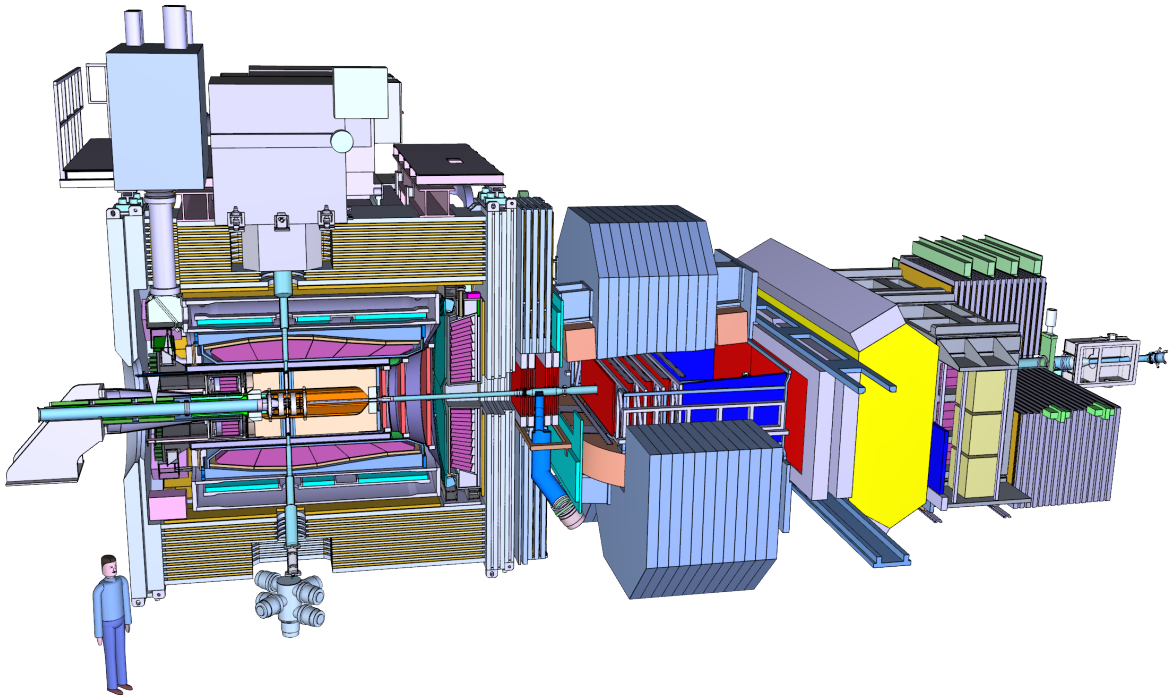

Figure 2.2: Cutaway 3D drawing of the full $\overline{\text{P}}$ANDA setup[1].

2.3 Electromagnetic Calorimetry

The EMC measures the energies of the photons and charged particles created in the collision. The portion of the EMC-subdetector within the TS is comprised of the forward and backward endcaps and the barrel. These, in total, contain about 16 000 crystals made from PWO-II, which make up the sensitive volume of the detector. The crystal distribution is 4 272 crystals in the forward endcap, ca. 500 in the backward endcap and 11 360 in the barrel [3]. Calorimetry in the FS is performed by a shashlyk type calorimeter [3] (see Figure 2.2 behind the RICH detector shown in yellow).

The crystals within the barrel are tapered to minimize empty spaces between crystals in the package and therefore reducing detection inefficiencies. Additionally, the crystals are not directly aimed at the interaction point, but rather 4° behind it, to eliminate possible particle paths that would otherwise pass through the wrappings between two adjacent crystals. In this case, these particles would not be detected. This scintillation light is then read out on the far side of the crystal by two Large-Area Avalanche Photodiodes (LAAPDs).

High energy particles entering the crystal excite the active centers of the lattice and deposited energy is released by the crystal through scintillation. The exact mechanism is complex but can generally be divided into three main processes: absorption and multiplication, energy carrier migration and relaxation/emission [4, 5].

- **Absorption/Multiplication**
  High energy particles interacting with the lattice knock an electron out of its inner shell and thus create a hole-electron pair. The high energy of the resulting electron dissipates by exciting more electrons. This process repeats until the energies of the electron in the shower is lower than the ionization energy of the scintillator. The electrons and the holes then thermalize to their respective band boundaries, forming free or self-trapped excitons.

[1] Clickable and annotated version: https://panda.gsi.de/panda

- **Energy carrier migration**
  In order to produce scintillation light, energy carriers first have to migrate to the luminescence centers of the doped scintillator. The energy transfer efficiency S to these centers is dependend on many factors such as crystal doping, defects and temperature. Effects of many of these are not fully understood and still an ongoing field of interest in scintillator optimizations.

- **Relaxation/Emission**
  Once the energy transfer to the luminescence centers has occurred, electrons and holes relax into excited dopant states which are located within the bandgap of the crystal material. These levels have to be chosen carefully by choosing dopant type and concentration to inhibit emission quenching. After the lifetime of these dopant is exceeded, a scintillation photon is created with a quantum efficiency Q.

The amount of generated scintillation light N_{gamma} is directly proportional to the number of electron hole pairs, depending on the transfer efficiency S and the quantum efficiency Q of the luminescent centers.[4]

$$N_{\gamma} \propto N_{e/h} S Q \tag{2.1}$$

Scintillation light is then internally reflected and subsequently collected by the two LAAPDs on the rearward face of the crystals. To further decrease the loss of scintillation light, especially for steep reflection angles inside the crystal where total internal reflection is no longer possible, the crystals are wrapped with several layers of Polytetrafluorethylene (PTFE) and reflective foil. Multiple crystals are then mounted in square alveoli made from carbon fibre, called a supermodule. Several supermodules are combined and mounted onto a support beam structure, making up one 'slice', 16 of which make up the complete barrel. The long slice sections can be seen in Figure 2.3.

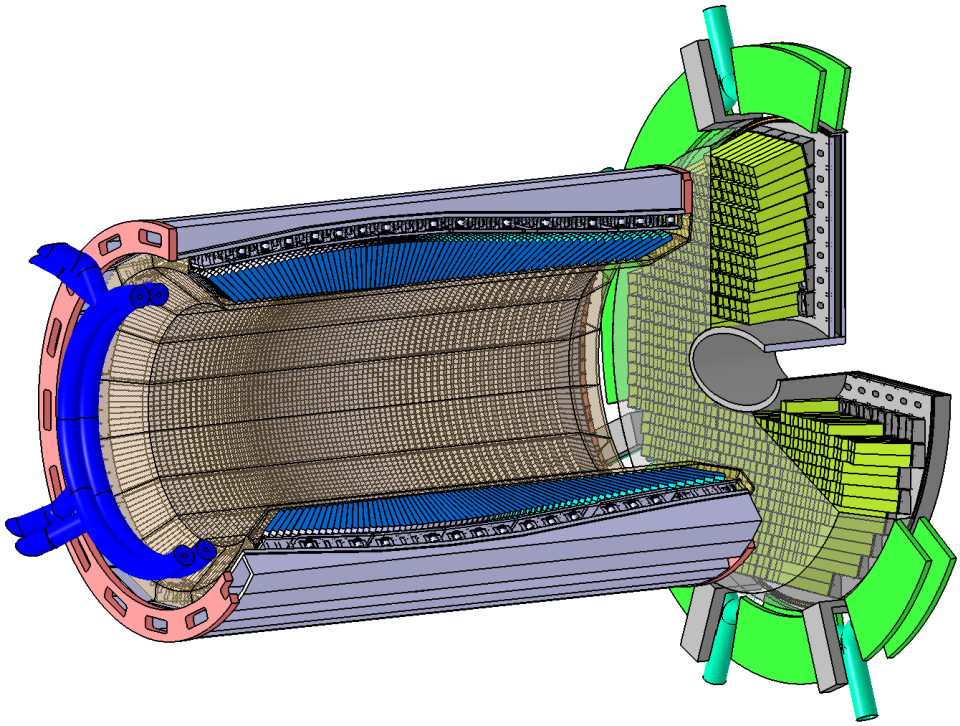

Figure 2.3: EMC barrel and forward endcap with accompanying support structure (backward endcap not shown).

2.4 Tapered Crystal Geometry

A cutaway drawing of the EMC barrel and forward endcap can be found in figure 2.3, the crosssection of a slice can also be seen. Figure 2.4 shows the slice crosssection in more detail and illustrates how crystals within a slice are focussed slightly behind the interaction point. Crystals need to be tapered on two sides to fully tile the barrel without gaps and to focus all crystals on this common focus point. In principle every crystal would need its own tapering angles, depending on the distance to the interaction point. As a simplification, the 71 crystals in a row in the longitudinal direction are grouped into 11 different crystal types. These types mainly differ in the strength of their tapering. In the transversal direction, two adjacent crystals are paired. They are mirror images of each other called the left and right handed form of one type. Close to the target point the tapering has to be the strongest since the opening angle for a given front face is larger the closer the crystals are to the center. At the far ends of the barrel the tapering is the least pronounced, due to the larger distance to the interaction point and therefore smaller opening angles.

The environment of the crystal imposes strict requirements on their optical parameters. A high production standard is mandatory and is achieved by pulling a cylindrical ingot from the $PbWO_4$ melt using the Czochralsky method. Crystals are then cut from the ingot, ground to shape, chamfered on the edges to prevent spalling and finally polished on all sides.

The light yield nonlinearity studied here is the most pronounced for strongly tapered crystals. Therefore, we will study only the crystal type 1. The dimensional specifications of the different crystal types are published in the $\overline{\text{P}}$ANDA Technical Design Report [6].

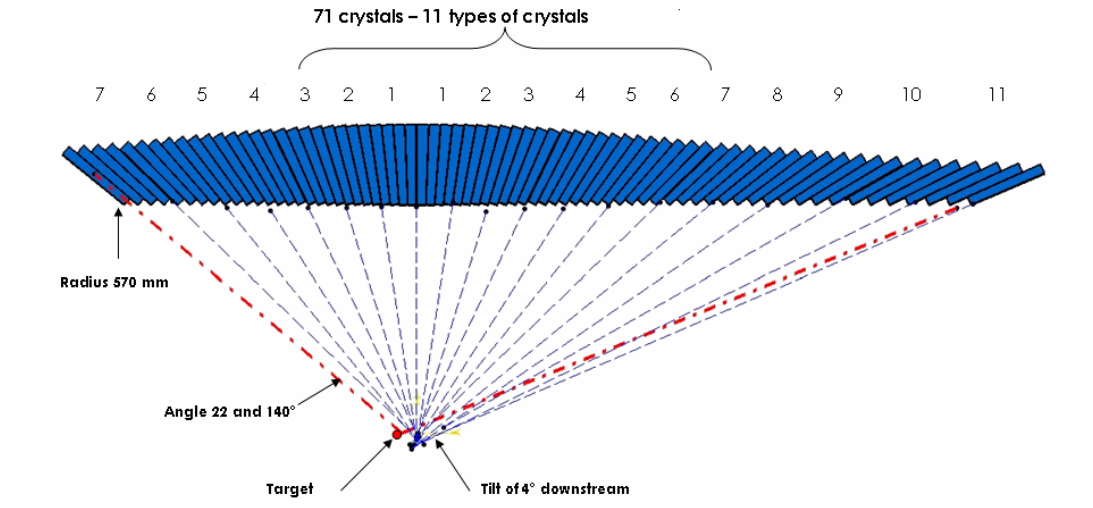

Figure 2.4: Cross section of a $\overline{\text{P}}$ANDA EMC slice, showing the focussing of crystals on their common focus point, which is located slightly behind the interaction point.

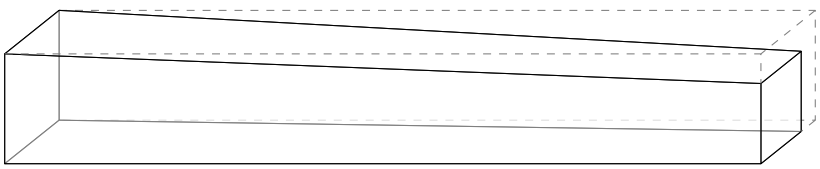

Figure 2.5: Crystal geometry of an EMC Type 1 crystal.

3 Light propagation in tapered crystals

Scintillation light, that is created in the crystal, is emitted isotropically by the excited crystal lattice and confined within that crystal primarily by total internal reflection. For incident angles that are greater than the critical angle of the PWO-II–air boundary, light is lost to the wrapping of the crystal. The first component of the crystal wrapping is several layers of Teflon foil, which was shown to have excellent diffuse reflectivity by Auffray et al. [7]. Any photons that manage to scatter through the Teflon are reflected back by the last layer of the crystal wrapping which is a highly specular reflective aluminized foil. The rear face is covered by LAAPDs instead of the wrapping and a small opening is left in the front face through which light can be guided into the crystal for calibration and radiation damage annealing.

3.1 Light Yield nonlinearity

The experimental ground work on light yield nonlinearity was done by Bremer [8] and Marteinsdóttir [9]. Bremer and Marteinsdóttir both experimentally measured the light yield along the crystals. Marteinsdóttir showed the significance of light yield nonlinearities in tapered crystals, which gave reason to model this effect in PandaRoot. They investigated the influences on energy resolution, energy leakage and Poisson statistics while Bremer used SLitrani simulations and experiments to investigate the cause and characteristics of the light yield nonlinearity. The tapered geometry was proven to be the main contributing factor for the nonlinearities, as the three tapering angles of the crystal faces correlate strongly with the light yield [8].

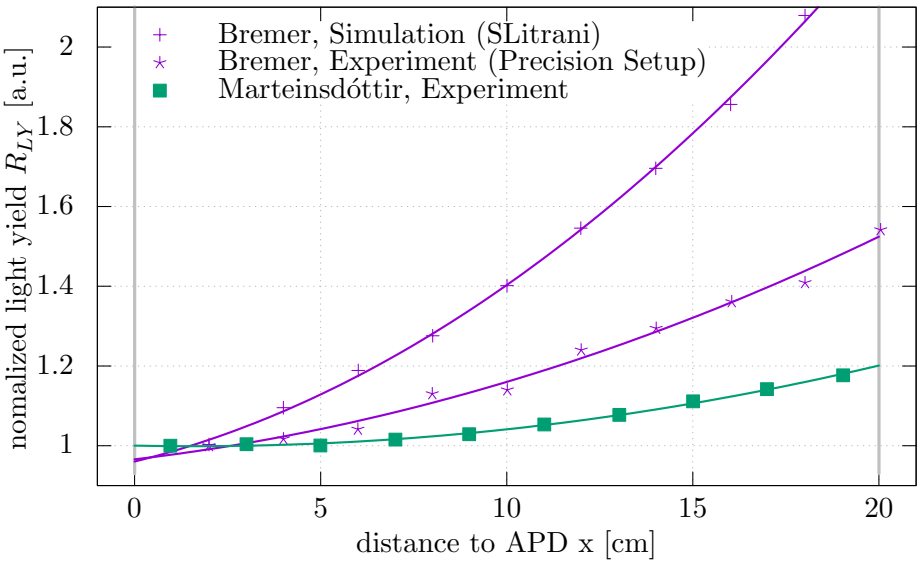

Figure 3.1: Normalized light yield data from Bremer [8] and Marteinsdóttir [9] for a Type 1 EMC crystal.

3.2 Simulations with p5.js

To obtain a notion for the character of the nonlinearity, a first principle simulation was developed using the p5.js creative coding JavaScript library. JavaScript and the p5.js library were chosen for their intuitive graphing capabilities, which made the development and debugging mroe visual and easy. The source code of the simulation is publically available on GitHub [10].

3.2.1 Naive Approach

The initial aim of this simulation was to estimate the number of different possible light paths, which eventually hit the APDs on the rear face of the crystal. To keep the simulation simple, a few idealizations were made:

- 2D only
- only total internal reflection is possible; rays with incident angles below the critical angle of $\theta_c = 27.44^\circ$ are never reflected and leave the crystal
- crystal has no wrapping; photons do not scatter back into the crystal once they leave the crystal
- transmittance in the crystal is 100%; the volume does not absorb photons

For these reasons, the simulation is a solely geometric consideration of light propagation within the crystal volume.

In Figure 3.2, three resulting visualizations of the simulation show the different regions in which light from a point source can propagate to. Paths in the two red areas above and below the source do not reach the APDs, as they immediately leave the crystal or are reflected into progressively steeper angles by the tapering and eventually, can no longer be totally reflected. Light rays in the red area to the right of the source fall onto the right crystal face in an angle too steep to result in total reflection. The dark blue area to the left of the source contains all paths that are emitted towards the APDs, while the light blue areas to the right contain the rays which are totally reflected on the top, bottom and right faces of the crystal before eventually reaching the APDs. The different shades of blue signify the different path lengths from the source to the APD, with dark blue marking short paths and light blue marking long paths.

3.2.2 Absorption and Reemission

So far, the simulation has only described an idealized behavior of light in a wrapped, slightly opaque crystal. To provide a more accurate description, the code was modified to model absorption in the material and reemission back into the crystal from light scattered into the wrapping.

The simulation first creates 10 000 rays at the origin with isotropic angular distribution and calculates a straight line to one of the crystal boundaries. Subsequent rays from reflection or reemission are aggregated in a path object containing all the individual segment rays until finally being absorbed by the APD, the material or the wrapping. If the incident angle of a ray on a crystal boundary is less than the critical angle $\theta_c = 27.44^\circ$, a new ray is created, mirrored at the surface normal of the boundary. If not, the ray leaves the crystal and interacts with the wrapping.

This interaction is implemented by generating a random number between 0 and 1 and comparing it to the wrappings reflectivity. For PTFE this reflectivity is 0.98 according to Auffray et al. [7] and even 0.99 according to Janecek [11]. If the random roll is higher than the reflectivity value, the ray is absorbed and terminated. For all rays that will be reemitted by the Teflon wrapping, a new ray is created with uniformly random angles in the range of $[-\theta_c, \theta_c]$.

Whether a light ray is absorbed in the crystal material or not, is calculated after all rays have been propagated to absorption. The $\overline{\text{P}}$ANDA PWO-II crystals show a transmittance of $T = \frac{I}{I_0} \approx 70\,\%$ at 430 nm over their whole length of 200 mm [12, 13, 14]. With

$$I = I_0 \exp(-\alpha x) \tag{3.1}$$

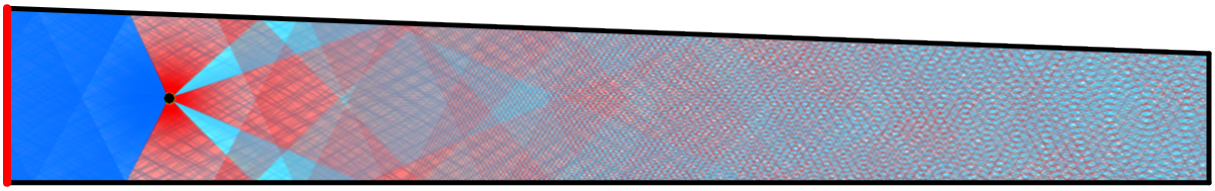

(a)

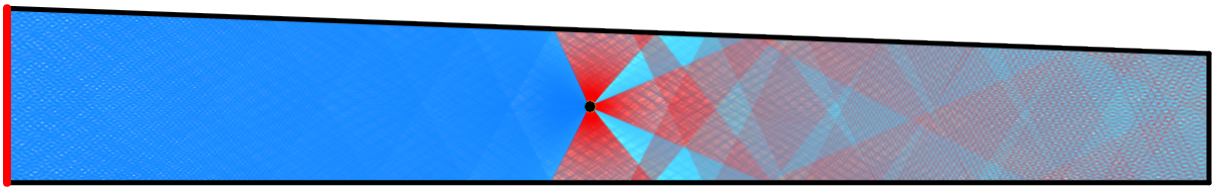

(b)

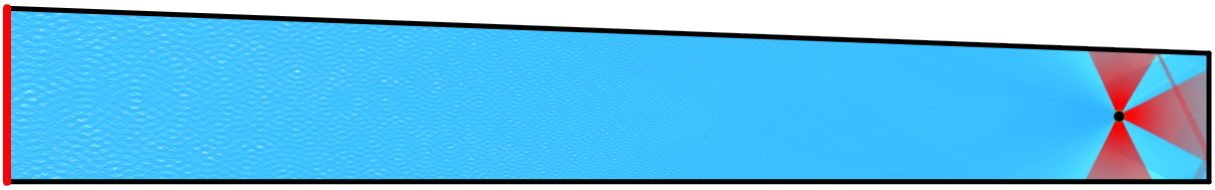

(c)

Figure 3.2: First principle simulation of light propagation inside tapered crystals. Configuration: no absorption, no wrapping. Light is isotropically produced at the black dot, centered at the crystal width. The rear crystal face which would have the APDs mounted to it with optical grease is shown in red on the left. The rays are colored from dark blue to light blue depending on the distance travelled until absorption. If a ray is unable to undergo total internal reflection, it is colored red.

the resulting absorption coefficient is $\alpha = 1.71\,\mathrm{mm}^{-1}$. To determine if a photon is absorbed, the path length is calculated and equation 3.1 is used to obtain the transmittance probability. Analogous to the implementation of the reemission from the wrapping, a random number is generated which determines if that ray is absorbed by the crystal volume or not. Where and why rays are terminated is counted and displayed to the user.

Some illustrative data from the simulations can be found in Table 3.1. The relative light yield normalized to the smallest value $R_{LY,norm}$ for all sampled positions and configurations is shown in Figure 3.3.

Configuration	$x[mm]$	$nRays$	$nAPD$	$nWrapping$	$nAbsorbed$	R_{LY}	$R_{LY,norm}$
no wrapping no absorption	30.7	10 000	4 764	5 236	0	0.4764	1.009
	100.0	10 000	4 979	5 021	0	0.4979	1.054
	169.3	10 000	5 336	4 664	0	0.5336	1.130
with wrapping with absorption	30.7	10 000	7 163	1 142	1 684	0.7163	1.134
	100.0	10 000	6 536	1 280	2 178	0.6536	1.035
	169.3	10 000	6 321	1 074	2 590	0.6321	1.001

Table 3.1: Example data from the simulation for three positions in the crystal. *nRays* total number of generated rays, *nAPD* number of rays that arrived at the APD, *nWrapping* number of rays getting stuck in the wrapping, *nAbsorbed* number of rays absorbed by the crystal.

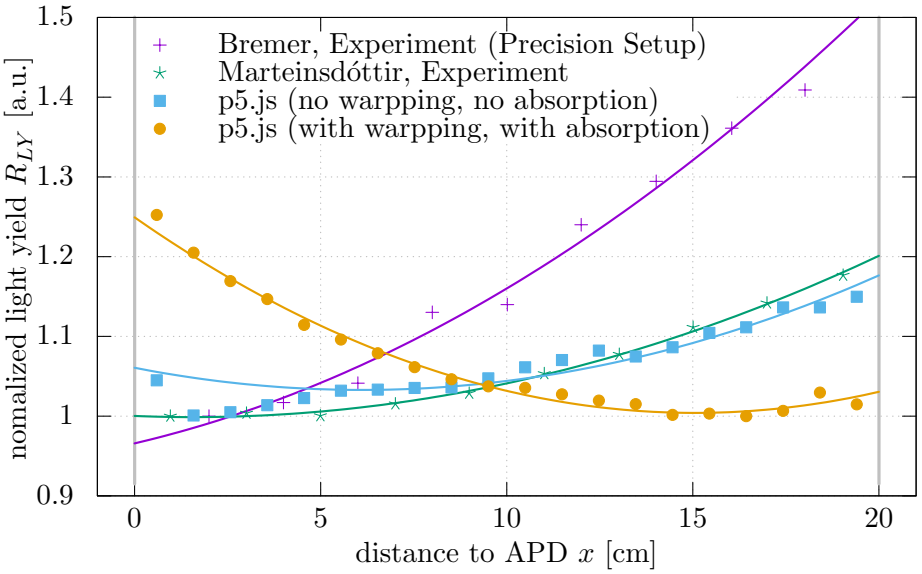

Figure 3.3: Light output at the APD sampled along the crystal length with different configurations in the p5.js simulation. Experimental data from Bremer and Marteinsdóttir as reference. The gray borders show the crystal boundaries. Fits are second degree polynomials.

3.2.3 Interpretation

Figure 3.3 shows the two p5.js simulations alongside the reference by Bremer. Looking at the graph without absorption or wrapping, one can see that the overall shape of the function is not too different from the reference, but for the far side of the crystal, too little light reaches the detector compared to the reference. However, the graph where absorption and the reflective

wrapping is taken into account is very different in overall shape. Too few light paths reach the detector from the far side when compared to the close side. In Figure 3.3 p5.js data shows $R_{LY,norm} = 1.14$ for $x = 19\,\text{cm}$ and experimental data by Bremer show $R_{LY,norm} = 1.48$. This indicates that the used absorption coefficient was too high, as other contributing factors such as the missing third dimension and inefficiencies are not taken into account.

Therefore, we will extend the code in the future into a small but capable tool to understand light transport inside scintillators. Thanks to my colleague Marvin Peter, the code has already been translated to C++[2]. The use of a dedicated optical simulation package is better suited for simulations with increasing requirements on accuracy, such as specific or multiple wavelengths, polarization or birefringence. However, the aim for this project is to provide a flexible system to estimate light collection behavior, specifically in scintillators.

[2] C++ version of the p5.js code: https://github.com/SimonGLM/p5-propagate/tree/cpp

4 PandaRoot Simulations

PandaRoot is a powerful framework which simulates the subdetectors and their responses to particles created by proton-antiproton-annihilation at the interaction vertex. It allows the development of particle identification (PID) algorithms using input data closely matching future experiment data. Conceptually, we can think of PandaRoot consisting of two separate regimes.

One is the simulation side, where particles are created, propagated, decayed and absorbed. A close approximation of the standard model and surrounding physics as we understand them today is implemented here. This is accomplished by Geant4 – a toolkit for simulating the passage of particles through matter [15]. It tracks particles through the sensitive subdetector volumes and creates hits in these detectors. Digitization algorithms then create realistic responses which replicate the electronics found in the physical detector. In PandaRoot these are called EMC Digis.

The other side is the reconstruction. Generated realistic detector responses are processed by detector specific algorithms to gather information about the particles which interacted with the detector.

> "In the central tracker a first track fit is performed using a conformal map transformation based on a helix assumption, then the track is used as input for a Kalman Filter (package genfit), using GEANE as track follower. The track is then correlated to the PID detectors (e.g. Cherenkov detectors, EM Calorimeter or Muon Chambers) to evaluate a global particle identification probability, using a Bayesian approach or multivariate methods." – Spartaro et.al. [16]

Using this information, the initial state which was generated during the $\overline{\mathrm{p}}$ annihilation at the target vertex can be reconstructed.

A primary design philosophy of PandaRoot is to use the reconstruction and analysis algorithms, which are developed using the simulated $\overline{\mathrm{P}}$ANDA, on the final physical detector, with only minimal changes. Additionally, PandaRoot will aid in the search for new physics by implementing new theoretical results and inferring reasonable detector responses, which can then help in finding the patterns in the data, proving the theories.

4.1 Data Acquisition Chain and Data Flow

The framework provides several different ways to generate particles and events. One of these is the `PndBoxGenerator` (aka particle gun), which can create packets of particles with arbitrary directions and momenta. They are then propagated and tracked using Geant4 and other packages included in FairSoft. The detector responses to these particles interacting with the sensitive detector volumes are created by digitizers, specific to each subdetector of the PANDA experiment. For example, the simulated raw detector response for the EMC happens on the level of individual waveforms produced by the LAAPDs and their frontend electronics. Multiple of these '`Hits`' are then processed into particle tracks or clusters, from which PID can be performed using several PID algorithms in the analysis part of PandaRoot.

4.1.1 The Code

Shown in Listing 4.1 are the relevant lines of code which are responsible for the light yield nonlinearity. First, we can see that nonuniformity parameters are retrieved for a specific `DetId` (line 430), which uniquely identifies the crystal in the EMC, and stored into the coefficient array

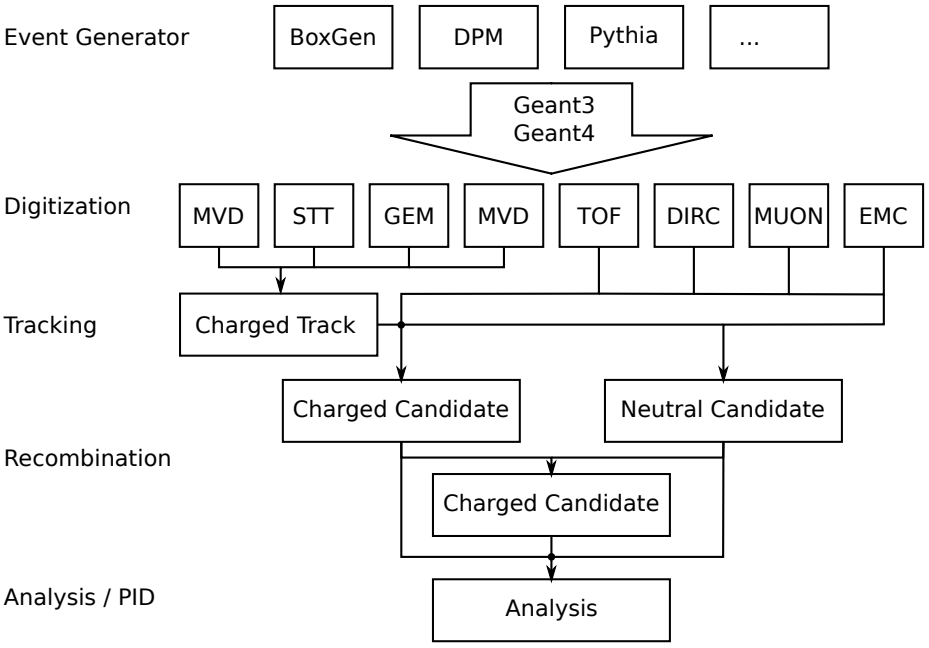

Figure 4.1: PandaRoot simulation data flow[16].

```
302 Double_t zpos;
303 Double_t energyscalefactor = 1.0;
304 Double_t c[3];
```

[...]

```
430 fNonuniformityPar->GetNonuniformityParameters(DetId, c);
431 energyscalefactor = c[0] + zpos * (c[1] + zpos * c[2]);
432 fShower[DetId][point->GetClusterID()] += point->GetEnergyLoss() *
        energyscalefactor;
433 fTrackEnergy[DetId] += point->GetEnergyLoss() * energyscalefactor;
```

Listing 4.1: The implementation of the nonuniformity in `PndEmcHitProducer::Exec()`.

`c[3]`. A second order polynomial is then used to calculate the `energyscalefactor` (line 431) depending on the position of the `Hit` within the crystal `zpos`.

$$energyscalefactor(z_{pos}) = c_0 + z_{pos} * (c_1 + z_{pos} * c_2) \tag{4.1}$$

$$= c_0 + c_1 z_{pos} + c_2 z_{pos}^2 \tag{4.2}$$

This factor is then used to scale the energy loss of one `point` (line 432, 433). A `point` is the Geant4 data object which is representing where particles have interacted with sensitive detector regions. It contains the energy the particle has deposited at that location.

4.2 Methodology of Measuring Light Yield

4.2.1 Challenges with PandaRoot

Unfortunately, PandaRoot does not track individual photons created by scintillation since this would be a huge computational overhead with little benefit to the accuracy of the simulation.

Instead, only the amount of deposited energy inside the crystal is used in modeling the detector response. For this reason, we cannot obtain the exact number of scintillation photons per deposited MeV. Thus, no light yield represented as photoelectrons per MeV (phe/MeV) can be determined. Since the number of photons created is directly proportional to the total energy deposited in the crystal (equation 2.1)[4], we can use the deposited energy to gain insight into the light yield nonlinearity implementation within PandaRoot.

4.2.2 Approach

As a practical approach to measure the light yield along the length of the crystal, the particle gun (PndBoxGenerator) code was modified to allow for arbitrary placement of the event generator origin, from where particles are created. The concerning changes can be found in the PandaRoot repository in the merge request `!263`[3].

In a simulation, the user generally has the benefit of knowing the absolute truth of what has happened. Within PandaRoot this information is stored in the MCTruth tree alongside with all the individual subdetector digitized data. This lets us compare what was measured by the detector (the Digis) versus what 'actually' happened (`MCTruth` in the `Hits`).

During analysis runtime we can then obtain all the particle tracks which are entering as well as exiting one particular crystal. Summing up the energies of these tracks yields the energy difference $E_{in} - E_{out} = E_{dep}$. As these tracks are part of the Monte Carlo Truth (MCTruth) we can reasonably assume that this difference is the amount of energy which was deposited in the crystal.

With this approach, the detected events would ideally be one particle entering and causing scintillation in the crystal. Then particles would either leave the crystal or a get stuck and deposit all their initial energy within the crystal.

Unfortunately, there are a couple of cases in which this overidealized assumption of these events does not hold. For example it is possible for nuclei and nucleons to get knocked out of the crystals, which leads to a negative deposited energy, as these nuclei carry away a large amount of rest mass energy. While this is physically accurate, it is not feasible to correct for this error by identifying and taking into account the energy carried away by these particles. Instead, it is easier to generate more events which then have another chance to match the following constraints:

- $E_{dep} > 0$
  Exclude events with negative energy deposited in the crystal. This is typically the case if material is knocked out of the crystal.

- $N_{tracks,entering} = 1$
  Exclude events with particles being scattered back into the crystal. This is typically the case if more than one particle has hit the crystal.

- The particle is primary
  Generated primary particles might interact or decay before entering the crystal. The entering particles are then flagged as secondary particles.

Events that do not satisfy these requirements are rejected at analysis time but are still preserved in the simulation data.

[3] https://git.panda.gsi.de/PandaRootGroup/PandaRoot/-/merge_requests/263

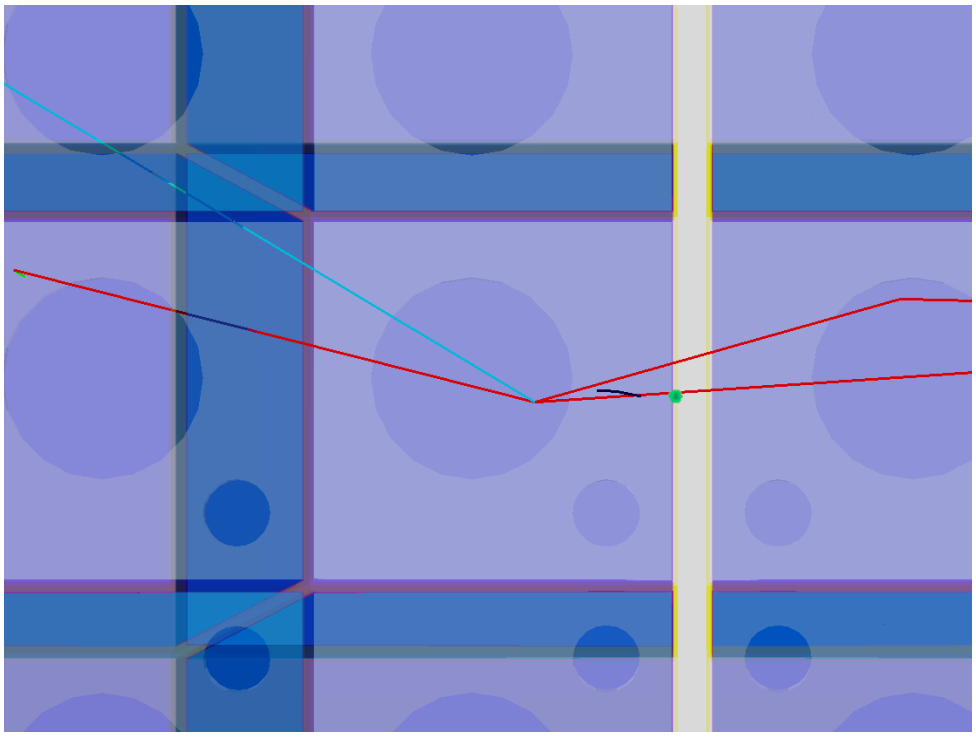

Figure 4.2: This view is a transparent drawing of the crystal from the outside of the barrel. The green dot represents the particle gun. Red paths are photons, the turquoise path is the neutrino from muon decay.

The position of the particle gun has to be defined at the beginning of simulation time and cannot be changed throughout. Therefore, several separate simulations were performed, each with the particle origin moved 1 cm along the crystal length.

4.2.3 Muon Decay as a Standard Candle

Due to the nature of the approach to probe the light yield, we are not really interested in the scintillation physics of any particular event. Our investigations merely requires a predictable lightsource in the crystal, which does not necessarily has to originate from $\overline{\mathrm{p}}$ p annhilation. Using particles at relativistic energies, which we mainly expect to see during experiments in the future physical detector, would result in many aforementioned 'dirty' events in the analysis due to backscattering and nuclei being knocked out of the crystal lattice.

In Table 4.1, we compare the rejection rates of the criteria given in Section 4.2.2 on various particles and energies. Key values to look at are the total number of generated digis 'digis-total' and the overall acceptance of the digis 'accepted-total'. A higher acceptance results in less simulated events needed for a given number of accepted events and thus, shorter compute time and quicker development iterations. Therefore, a high number 'accepted-total' and a low number of total digis created in the simulation is highly desireable.

As we can see in Table 4.1, low muon momenta yielded the highest event acceptance after filtering. We therefore chose the muon momentum to be $p_\mu = 80\,\mathrm{MeV}$ for the rest of this work.

Particle	μ^-				
Energy	50 MeV	80 MeV	100 MeV	500 MeV	1 GeV
digis-total	209 666	197 457	197 332	156 9258	2 882 360
multiple-entering [%]	9.72	9.41	9.56	0	0
multiple-hits-in-digi[%]	0	0	0	0	0
negative-E_dep [%]	17.06	18.32	18.21	< 0.01	0
no-entering [%]	0	0	0	0	0
no-hit-in-digi [%]	< 0.01	< 0.01	< 0.01	< 0.01	< 0.01
no-primary [%]	0	0	0	0	0
not-in-114crystal [%]	52.96	49.36	49.32	93.63	96.53
primary-exiting [%]	0.01	< 0.01	< 0.01	6.37	3.47
acceptance [%]	20.26	22.91	22.90	0	0
accepted-total	42 469	45 247	45 192	0	0

Table 4.1: Rejection percentages and reasons for rejection of all digis created.

Energy loss in a material is given by the Bethe formula

$$-\frac{dE}{dx} = \frac{2\pi n z^2 e^4}{m_e v^2}\left\{\ln\left(\frac{2m_e v^2 W_m}{I^2(1-\beta^2)}\right) - 2\beta^2 - \delta - U\right\} \tag{4.3}$$

where W_m is the maximum transferable energy to atomic electrons, I is the mean excitation energy of the material and $-\delta$ and $-U$ are correction terms which will not be discussed further. A full discussion of the derivation and the individual terms is given in [5]. We will now only discuss the stopping power or energy loss

$$S(T) = -\frac{dE}{dx} \tag{4.4}$$

as the numerical data obtained by the Particle Data Group [17] (PDG). Figure 4.3a shows the energy loss of muons in $PbWO_4$ using data from [18] and with the chosen $p_\mu = 80\,\text{MeV}$ ($T_\mu = 26.9\,\text{MeV}$) the energy loss amounts to circa[4] $S(T) = 18.9\,\text{MeV}\,\text{cm}^{-1}$. The CSDA ranges is the inverse integral of the stopping power summing up the energy loss until the particle lost its kinetic energy.

$$R(T_0) = \int_0^{T_0} \frac{1}{S(T)}\,dT \tag{4.5}$$

$$R(26.9\,\text{MeV}) = 0.865\,\text{cm} \tag{4.6}$$

The range $R(26.9\,\text{MeV})$ at which the muons are stopped, lies roughly at the center of the PWO-II crystals which have a width of about 2 cm. The stopped muons eventually decay, producing a Hit in the detector.

4.3 Analysis

The filtering and analysis of the events is done by utilizing a C++ script specifically developed for this purpose and executed by ROOTs own C++ interpreter CINT. This script loops over every simulated event, filters for the criteria previously explained and extracts the key metrics. The metrics which are extracted and aggregated into histograms include:

[4] Intermediate values are linearly interpolated.

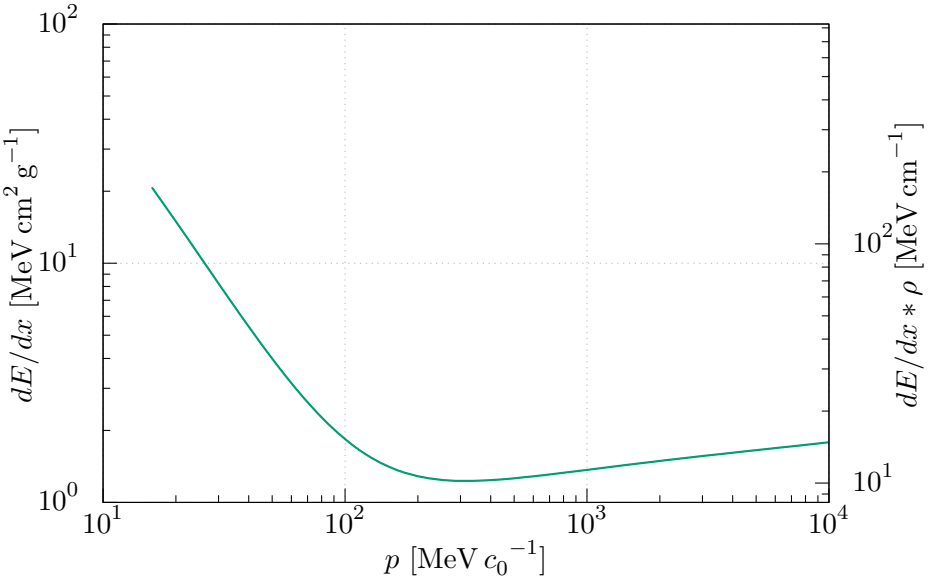

(a) Energy loss of muons in $PbWO_4$.

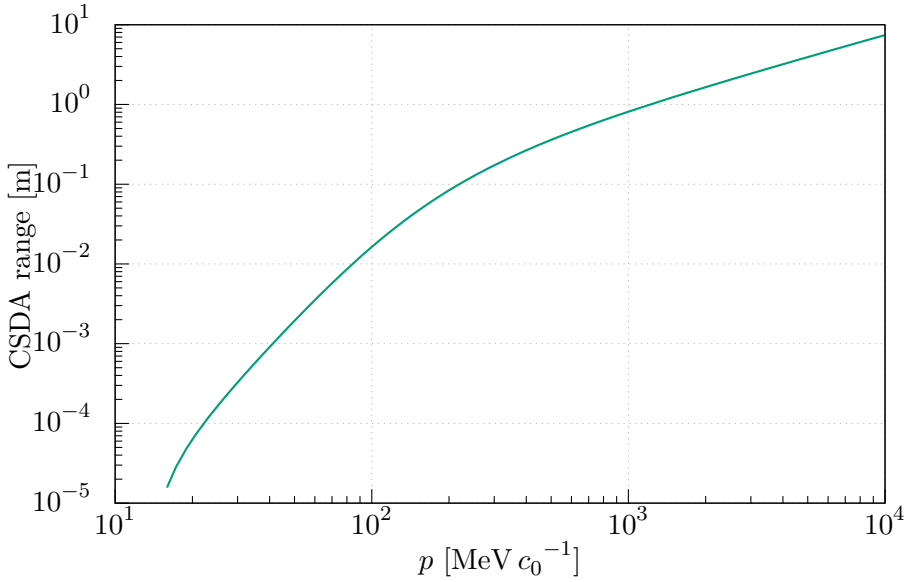

(b) CSDA range of muons in $PbWO_4$.

Figure 4.3: Muon energy loss function and CSDA range of muons in lead tungstate ($PbWO_4$) with data from the PDG [18].

- X_{fit}: the interaction position along the crystal length
- $E_{dep} = E_{in} - E_{out}$: deposited energy
- E_{digi}: the energy measured by the EMC
- $R_{LY} = E_{digi}/E_{dep}$: the ratio between E_{digi} and E_{dep}

Looking at the graphs for the position $x = 10\,\text{cm}$ in Figure 4.4, we can see the histogram of E_{digi} (Fig. 4.4b) is similar in shape but laterally shifted compared to E_{dep} (Fig. 4.4a). The behavior of the shift is the effect of the scaling in the code (Listing 4.1). These individual values are then divided by one another and filled into the R_{LY} histogram (Fig. 4.4c), the peak of which is then fitted with a gaussian to determine the peak's position more precisely than just the maximum value. This is repeated for all positions sampled and plotted in Figure 4.5 along with the data obtained by Bremer [8].

In Figure 4.5 can see that the graph obtained from the PandaRoot simulation is substantially lower than the experimental data by Bremer. However, the PandaRoot data agrees very well with the results by Marteinsdóttir. If Bremer's data is assumed to be correct, the discrepancy to the data obtained from PandaRoot is quite significant. This suggests a large discrepancy in the amount of light measured in the simulation versus the amount of light measured in experiments or the future physical detector. The implications of this are further explained in Section 5. If, however, the data by Marteinsdóttir is correct, experiment and PandaRoot agree quite well.

Curiously, the PandaRoot data matches the p5.js simulation data without wrapping or absorption remarkably well (Figure 4.6). However, since the p5.js data without wrapping or absorption does not precisely represent the actual setup, this comparison holds little value for interpretations about the correctness of the light yield nonlinearity data from PandaRoot.

4.4 Latest PandaRoot version

FairRoot and PandaRoot are still under active development. As of August 15, 2022 the latest PandaRoot version available is `v13.0.0`.

The currently used versions are:

- gcc `8.4.0`
- cmake `3.16.3`
- FairSoft `apr22`
- FairRoot `v18.6.8`
- PandaRoot `v13.0.0`

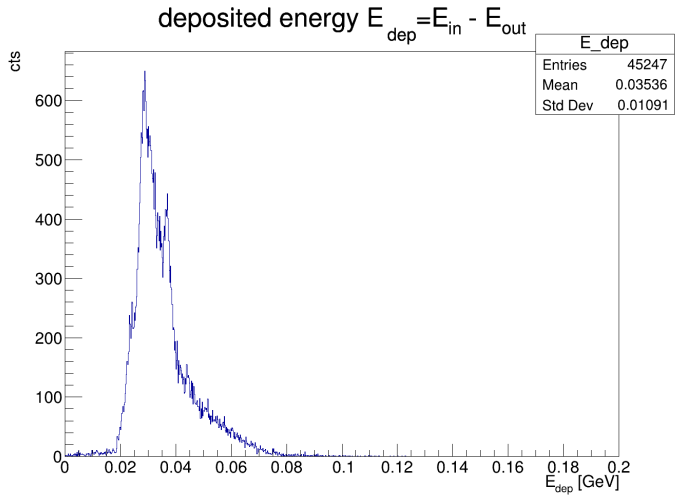

(a) Energy actually deposited in the crystal.

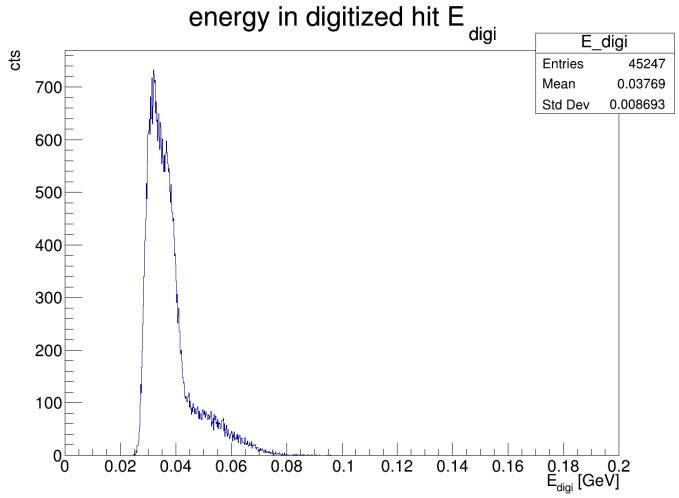

(b) Energy digitized by the readout algorithms.

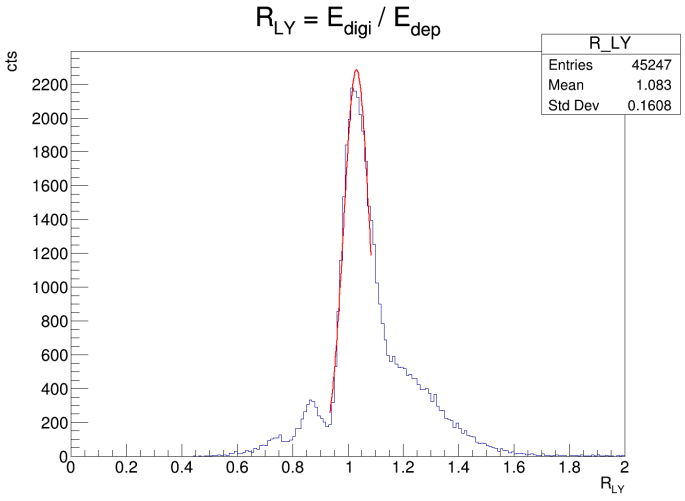

(c) Ratio of measured versus deposited energy.

Figure 4.4: Relevant metrics plotted for position $x = 10\,\mathrm{cm}$.

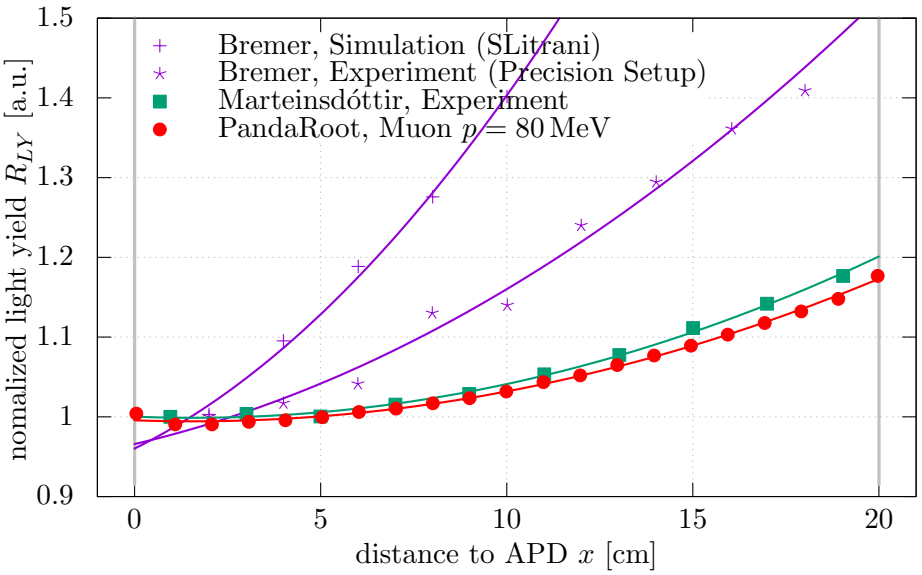

Figure 4.5: Comparison of PandaRoot data and experiment data. Light yield measured at various positions along the crystals length, normalized to the smallest value. Note the discrepancy between PandaRoot data and experiments by Bremer, but the close agreement to data by Marteinsdóttir. Gray vertical lines represent the physical boundaries of the crystal.

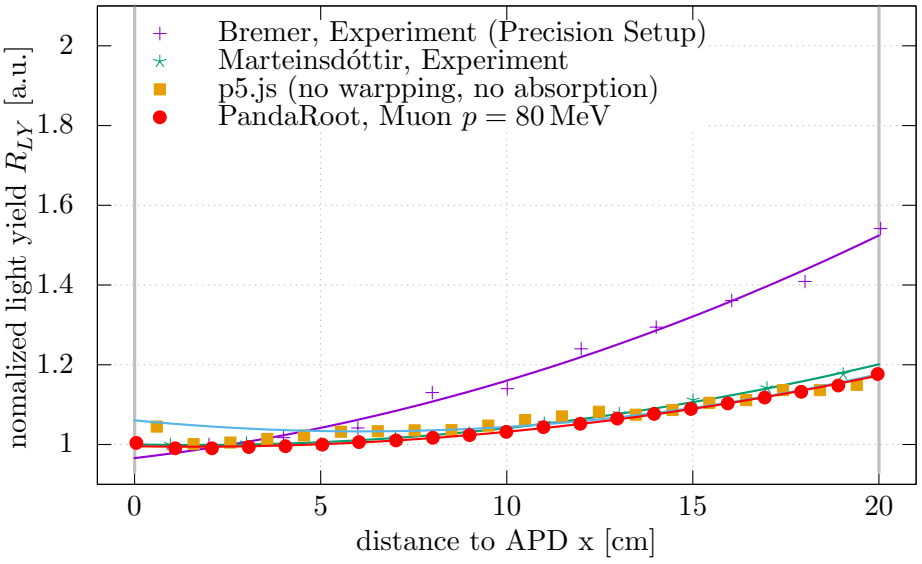

Figure 4.6: Comparison of PandaRoot data and p5.js data. Note the naive p5.js simulation (yellow) fits well to the experiment by Marteinsdóttir and the PandaRoot data.

5 Results and Conclusion

The aim of this work was to validate the light yield nonlinearity implementation in the PandaRoot framework. Understanding and modeling realistic light propagation within the $\overline{\text{P}}$ANDA EMC crystals is essential for accurate and reliable PID.

As has been shown in this work, and in particular in Figure 4.5, the current implementation does not fit the experimental data obtained by Bremer [8]. The discrepancy of the light yield modeled in PandaRoot and the experimental data is largest for scintillation at far distances from the LAAPDs. Since particles with low energies do not penetrate the crystal as deep as higher energies do (Figure 4.3b), the mismatch between of measured and exact energy deposited is largest, for particles with comparatively low energies. With the EMC providing essentially wrong information about the measured particles, accurate contributions by the EMC to the overall $\overline{\text{P}}$ANDA PID accuracy cannot be relied upon.

However, PandaRoot data fits the work from Marteinsdóttir quite excellently. With respect to this dataset the validation was indeed successful and PandaRoot is accurate.

Therefore, we are unable to come to a final conclusion on the validity of the current implementation. Further investigations are necessary to determine which of the datasets is accurate and should form the basis of the light yield nonlinearity implementation in PandaRoot.

If the implementation is indeed faulty, a thorough audit of the code should be done. Following the inheritance chain and a data flow from loading of the nonlinearity coefficients from disk to the eventual use in the `PndEmcHitProducer`. The relevant files containing the coefficients for all crystal types seem to be either `EmcDigiNoniformityPars.root` or `EmcDigiNoniformityPars2.root`. Another approach is to adjust the coefficients until parity with experimental data is achieved. As mentioned, this would require more experimental research on the light yield nonlinearity with the final crystal setup including PTFE wrapping, two LAAPDs and all other relevant components of the system for every crystal type. One can then compare this data to the nonlinearity observed in PandaRoot.

The code developed for and used in this thesis is publicly available at GitHub [19].

List of Figures

Acronyms

$\overline{\text{P}}$ANDA Antiproton Annhilation at Darmstadt. i, ii, I, III, 1, 3, 4, 6, 8, 13, 23

APD Avalanche Photodiode. 1, 8, 10

APPA Atomic, Plasma Physics and Applications. 1

CBM Compressed Baryonic Matter. 1

CR Collector Ring. 3

DIRC Detection of Internally Reflected Cherenkov light. 3

EMC Electromagnetic Calorimeter. i, ii, I, III, 1, 3, 4, 6, 7, 13, 19, 23

FAIR Facility for Antiproton and Ion Research. i, ii, I, 1, 3

FS Forward Spectrometer. 3, 4

GSI Gesellschaft für Schwerionenforschung. i

HESR High Energy Storage Ring. 3

LAAPD Large-Area Avalanche Photodiode. 4, 5, 7, 13, 23

MVD Micro-Vertex-Detector. 3

NUSTAR Nuclear Structure, Astrophysics and Reactions. 1

PDG Particle Data Group [17]. I, 17, 18

PID particle identification. 13, 23

PTFE Polytetrafluorethylene. 5

STT Straw Tube Tracker. 3

TS Target Spectrometer. 3, 4

VMC Virtual Monte Carlo. 1

Glossary

alveoli A square carbon honeycomb made from thin carbon fibre to mount a package of crystals onto the rear support structure. 5

CSDA range Continuous slowing down approximation range. A very close approximation to the average path length traveled by a charged particle as it slows down to rest, calculated in the continuous-slowing-down approximation. In this approximation, the rate of energy loss at every point along the track is assumed to be equal to the total stopping power. Energy-loss fluctuations are neglected. The CSDA range is obtained by integrating the reciprocal of the total stopping power with respect to energy. [20] I, 17, 18

Digi A Digi is the digitized representation of a Hit the frontend electronics create in the $\overline{\text{P}}$ANDA EMC. 13, 15

Geant4 A software platform for the simulation of particle-matter interactions [15]. 13, 14

Hit A Hit is a data object inside PandaRoot, containing the MCTruth about all particles interacting in one EMC crystal. III, 13–15, 17

MCTruth The Monte Carlo Truth information is the mathmatical reality which was generated during the simulation. III, 15

PWO Scintillator material consisting of lead tungstate $PbWO_4$ used in the CERN CMS. III

PWO-II Improved version of PWO crystal material doped with molybdenum and lanthanum [6, 13]. 1, 4, 7, 8, 17

SIS100 Heavy ion sychrotron (ger.: Schwerionensynchrotron) with 100 T m bending power. 3

SLitrani SuperLitrani light transport package (discontinued) 7

References

[1] K Knie et al. „Concept for the Antiproton Production Target at FAIR“. In: *Conf. Proc.* C1205201 (2012), WEPPD030. 3 p. URL: https://cds.cern.ch/record/1558377.

[2] Alfons Khoukaz. „Internal targets for the PANDA experiment“. In: *PoS* STORI11 (2012), p. 036. DOI: 10.22323/1.150.0036. URL: https://doi.org/10.22323/1.150.0036.

[3] PANDA Collaboration. „Technical Design Report“. In: (2020). URL: https://panda.gsi.de/system/files/user_uploads/heinsius%40ep1.rub.de/RE-TDR-2020-007.pdf.

[4] G. Bizarri. „Scintillation mechanisms of inorganic materials: From crystal characteristics to scintillation properties“. In: *Journal of Crystal Growth* 312.8 (2010). The 17th American Conference on Crystal Growth and Epitaxy/The 14th US Biennial Workshop on Organometallic Vapor Phase Epitaxy/The 6th International Workshop on Modeling in Crystal Growth, pp. 1213–1215. ISSN: 0022-0248. DOI: https://doi.org/10.1016/j.jcrysgro.2009.12.063. URL: https://www.sciencedirect.com/science/article/pii/S0022024809011609.

[5] Claude Leroy and Pier-Giorgio Rancoita. *Principles of Radiation Interaction in Matter and Detection*. 4th. WORLD SCIENTIFIC, 2016. DOI: 10.1142/9167. eprint: https://www.worldscientific.com/doi/pdf/10.1142/9167. URL: https://www.worldscientific.com/doi/abs/10.1142/9167.

[6] PANDA Collaboration. „Technical Design Report". In: (2008). URL: https://panda.gsi.de/system/files/user_uploads/u.kurilla/RE-TDR-2008-001.pdf.

[7] E. Auffray et al. „A Comprehensive & Systematic Study of Coincidence Time Resolution and Light Yield Using Scintillators of Different Size and Wrapping". In: *IEEE Transactions on Nuclear Science* 60.5 (2013), pp. 3163–3171. DOI: 10.1109/TNS.2013.2270089. URL: https://doi.org/10.1109/TNS.2013.2270089.

[8] Daniel A. Bremer. „Measurements and Simulations on Position Dependencies in the Response of Single PWO Crystals and a Prototype for the PANDA EMC". dissertation. Justus-Liebig-Universität Gießen, 2014. URL: http://geb.uni-giessen.de/geb/volltexte/2014/10582/.

[9] María Marteinsdóttir. „Light Yield Nonuniformity in PWO Scintillators". In: (2009). URL: https://panda-wiki.gsi.de/foswiki/pub/EMC/LightYieldNonUniformity/light-uniformity-MMMaster_final.pdf.

[10] Simon Glennemeier-Marke. *p5.js geometric ray casting simulation repository*. 2022. URL: https://github.com/SimonGLM/p5-propagate (visited on 10/14/2022).

[11] Martin Janecek. „Reflectivity Spectra for Commonly Used Reflectors". In: *IEEE Transactions on Nuclear Science* 59.3 (2012), pp. 490–497. DOI: 10.1109/TNS.2012.2183385.

[12] Fan Yang et al. „A Study on Radiation Damage in PWO-II Crystals". In: *IEEE Transactions on Nuclear Science* 60.3 (2013), pp. 2336–2342. DOI: 10.1109/TNS.2013.2262660.

[13] R. W. Novotny et al. „Pre-Production of PWO-II Crystals for the PANDA-EMC". In: *2017 IEEE Nuclear Science Symposium and Medical Imaging Conference (NSS/MIC)*. 2017, pp. 1–5. DOI: 10.1109/NSSMIC.2017.8532973.

[14] Andrei Borisevich et al. „New Start of Lead Tungstate Crystal Production for High-Energy Physics Experiments". In: *IEEE Transactions on Nuclear Science* 63.2 (2016), pp. 569–573. DOI: 10.1109/TNS.2015.2505716.

[15] S. Agostinelli et al. „Geant4—a simulation toolkit". In: *Nuclear Instruments and Methods in Physics Research Section A: Accelerators, Spectrometers, Detectors and Associated Equipment* 506.3 (2003), pp. 250–303.

[16] Stefano Spataro and. „The PandaRoot framework for simulation, reconstruction and analysis". In: *Journal of Physics: Conference Series* 331.3 (Dec. 2011), p. 032031. DOI: 10.1088/1742-6596/331/3/032031. URL: https://doi.org/10.1088/1742-6596/331/3/032031.

[17] Particle Data Group. URL: https://pdg.lbl.gov/.

[18] Particle Data Group. *Atomic and Nuclear Properties*. 2022. URL: https://pdg.lbl.gov/2022/AtomicNuclearProperties/ (visited on 10/14/2022).

[19] Simon Glennemeier-Marke. *PandaRoot light yield nonlin studies repository*. 2022. URL: https://github.com/SimonGLM/PandaRoot_LY_nonlin_study (visited on 10/14/2022).

[20] National Institute of Standards and Technologies (NIST). *Appendix: Significance of Calculated Quantities*. URL: https://physics.nist.gov/PhysRefData/Star/Text/appendix.html (visited on 10/14/2022).

Selbstständigkeitserklärung

Hiermit versichere ich, die vorgelegte Thesis selbstständig und ohne unerlaubte fremde Hilfe und nur mit den Hilfen angefertigt zu haben, die ich in der Thesis angegeben habe. Alle Textstellen, die wörtlich oder sinngemäß aus veröffentlichten Schriften entnommen sind, und alle Angaben die auf mündlichen Auskünften beruhen, sind als solche kenntlich gemacht. Bei den von mir durchgeführten und in der Thesis erwähnten Untersuchungen habe ich die Grundsätze gute wissenschaftlicher Praxis, wie sie in der ‚Satzung der Justus-Liebig-Universität zur Sicherung guter wissenschaftlicher Praxis' niedergelegt sind, eingehalten. Gemäß § 25 Abs. 6 der Allgemeinen Bestimmungen für modularisierte Studiengänge dulde ich eine Überprüfung der Thesis mittels Anti-Plagiatssoftware.

Datum	Unterschrift